Branching ratio for the $M1$ decay of the $2\,^2S_{1/2}$ state in one-electron krypton

S. Cheng, H. G. Berry, R. W. Dunford, D. S. Gemmell, E. P. Kanter, and B. J. Zabransky
Physics Division, Argonne National Laboratory, Argonne, Illinois 60439

A. E. Livingston
Department of Physics, University of Notre Dame, Notre Dame, Indiana 46556

L. J. Curtis
Department of Physics and Astronomy, University of Toledo, Toledo, Ohio 43606

J. Bailey and J. A. Nolen, Jr.*
National Superconducting Cyclotron Laboratory, Michigan State University, East Lansing, Michigan 48824
(Received 24 August 1992)

We report a measurement of the lifetime of the $2\,^2S_{1/2}$ state in one-electron krypton and a direct determination of the branching ratio for the $M1$ decay of this state. The branching-ratio measurement provides a sensitive test of the relativistic corrections to the decay rate. The lifetime measurement yields (36.8±1.4) ps and the branching ratio is found to be 0.356(15), both in good agreement with the theoretical values of 37.008 ps and 0.3643, respectively. From these measurements we also deduce the corresponding magnetic-dipole decay rate $A_{M1}=9.68(55)\times10^9\ s^{-1}$ and the two-photon decay rate $A_{2E1}=1.750(78)\times10^{10}\ s^{-1}$.

PACS number(s): 32.70.Fw, 31.30.Jv, 31.10.+z

I. INTRODUCTION

The increasing availability of intense beams of highly charged few-electron ions at heavy-ion accelerators provides an opportunity for testing relativistic corrections to the energy levels and lifetimes of these ions. One of the most fundamental lifetimes is that of the $2\,^2S_{1/2}$ level in one-electron ions. This level decays to the $1\,^2S_{1/2}$ ground state either by two-photon emission or by single-photon $M1$ emission (see Fig. 1). The two-photon decay rate dominates at low nuclear charge Z. In fact, the $M1$ matrix element vanishes if nonrelativistic wave functions are used since the operator acts only on the angular parts of the wave functions and the radial parts are separately orthogonal. The $M1$ decay is therefore a completely relativistic phenomenon. The branching ratio for this decay increases with Z and becomes equal to the two-photon decay rate at about $Z=41$.

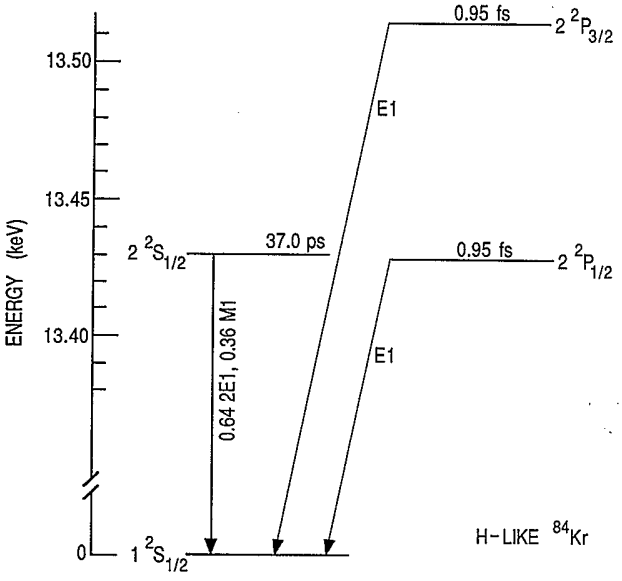

FIG. 1. Energy levels and lifetimes for the $n=1$ and $n=2$ levels of one-electron $^{84}Kr^{35+}$.

Precise nonrelativistic (NR) calculations of the two-photon decay rate have been given by Klarsfeld [1] and Drake [2]. Drake's value is

$$A_{2E1}^{NR}=8.229\,38Z^6\ s^{-1}\ . \tag{1}$$

Johnson [3] calculated the $M1$ matrix element in the Dirac theory and evaluated it in the nonrelativistic limit to obtain

$$A_{M1}^{NR}=2.496\times10^{-6}Z^{10}\ s^{-1} \tag{2}$$

for the "nonrelativistic" $M1$ decay rate. For krypton ($Z=36$), Eqs. (1) and (2) yield a lifetime of 36.982 ps and a branching ratio

$$b^{NR}=\frac{A_{M1}^{NR}}{A_{M1}^{NR}+A_{2E1}^{NR}}=0.3375\ . \tag{3}$$

Fully relativistic calculations [4–6] give a lifetime of 37.008 ps and a branching ratio

$$b^{rel}=0.3643\ . \tag{4}$$

Although the relativistic value for the lifetime is (accidentally) nearly equal to the nonrelativistic result, the relativistic value for the branching ratio is larger by 8%. Thus a measurement of the $M1$ branching ratio in Kr^{35+} provides a sensitive test of relativistic corrections to the decay rates.

The lifetime of the $2\,^2S_{1/2}$ level in one-electron ions has been previously measured to a precision of about 1% in He^+ [7,8], Ar^{17+} [9], and Ni^{27+} [10], and to lower precision in O^{7+}, F^{8+} [11], and S^{15+} [12]. The Ar^{17+} experiment was sensitive to the contribution of the magnetic-dipole amplitude to the total decay rate, and the Ni^{27+} measurement was sensitive to the relativistic corrections to the two-photon amplitude. In this paper we describe a measurement in $^{84}Kr^{35+}$ of the lifetime of the $2\,^2S_{1/2}$ level and a direct measurement of the $M1$ branching ratio.

II. EXPERIMENT

In the experiment, a beam of 30-MeV/amu $^{84}Kr^{15+}$ ions from the K1200 cyclotron at the National Superconducting Cyclotron Laboratory (NSCL) was stripped in a 3.4-mg/cm^2 aluminum target. The relative intensities of the 34+, 35+, and 36+ charge states in the emerging beam were in the ratio 40:47:13, respectively. The fully stripped $^{84}Kr^{36+}$ ions were selected and directed to our experimental chamber, where some of the ions were formed in the H-like $2\,^2S_{1/2}$ level by electron pickup in a carbon foil. The maximum beam current of fully stripped ions delivered to our chamber was 6 nA (electrical), but this beam was then collimated and attenuated to reduce backgrounds in our x-ray detectors.

The experimental chamber was optically aligned with the beam axis and the beam alignment was checked during tuning by viewers located before and after the target chamber. The beam current was monitored using a shielded beam dump located 5 m downbeam of the target chamber. This current was used to normalize the data.

The lifetime of the $2\,^2S_{1/2}$ state was measured by the beam-foil time-of-flight method, in which the target foil was moved relative to three fixed, collimated Si(Li) detectors (see Fig. 2). The intensity of the decay radiation was measured as a function of the foil position. The small decay length of the state (2.7 mm) provided a challenge in this measurement. It was necessary to observe the decay radiation within 1–2 mm of the foil in order to get a reasonable statistical accuracy without allowing the detectors to look directly at the beam spot on the foil. In order to achieve this, a special geometry was chosen, in which the beam passed through a "shield" (see Fig. 2 inset) before entering the detection region. The shield served to block the detectors from viewing the beam at the foil while allowing them to view the region a few millimeters downbeam of the foil. Detectors 1 and 2 were placed close to the beam and had a relatively unconstrained view downbeam of the shield. This maximized the solid angle and the coincidence rate. Detector 3 was more highly collimated so as to minimize the Doppler width but at the price of a reduced solid angle.

Three different foils of thicknesses 30, 95, and 188 μg/cm^2 were used in the interaction region. For the same current, the yield of ions in the $2\,^2S_{1/2}$ state for the 95-μg/cm^2 foil was about three times that of the 30-μg/cm^2 foil and only slightly less than that of the 188-μg/cm^2 foil. We chose to use the 95-μg/cm^2 foil since the radiation background was higher for the thicker foil.

Specifications of the Si(Li) detectors are given in Table I. Detectors 1 and 2 are nearly identical, whereas detector 3 has a thicker, larger-diameter window. Detectors 1 and 2 were fitted with 100-μm-thick Mylar filters to cut off low-energy x rays. All detectors were calibrated using x-ray lines from radioactive sources including ^{55}Fe, ^{57}Co, and ^{65}Zn. A typical calibration spectrum using the ^{55}Fe source is shown in Fig. 3.

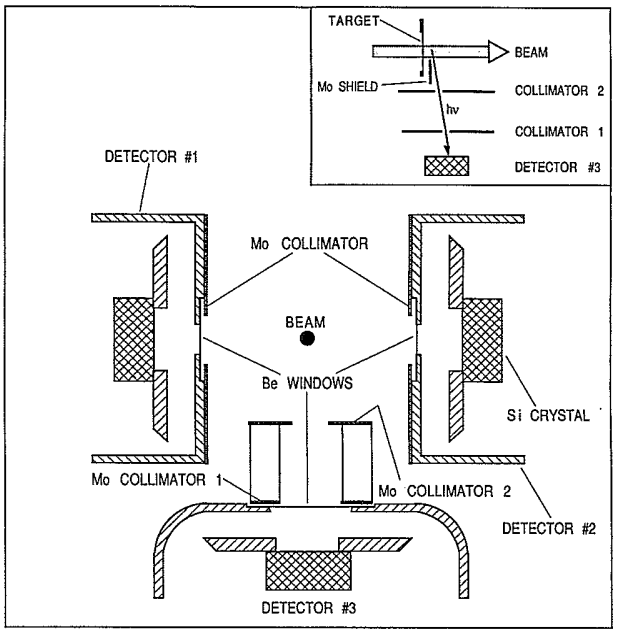

FIG. 2. Experimental setup showing the three Si(Li) detectors viewing the beam (axis perpendicular to page). Refer to Table I for relevant dimensions. The inset shows the tight collimation for detector 3. The Mo shield prevents the detectors from viewing the beam spot at the target foil.

The shield and detector collimators are made of 0.254-mm molybdenum sheets. This material was chosen because there are no characteristic x rays in the spectral region of interest for this experiment ($K\alpha$, 17.44 keV; $K\beta$ 19.60 keV; L x rays, 2.29–2.62 keV).

TABLE I. Detector geometry and characteristics. NA denotes not applicable.

	Detectors 1 and 2	Detector 3
Detector dimensions (mm)		
Active diam. (Si crystal)	9.7	10
Sensitive depth (Si crystal)	5.33, 5.15	5.27
Be window diam.	4.8	11
Si crystal to Be window	7	7
Beam to Si crystal	22.5	33
Collimator 1 slit[a]	3.2×6.25	2.5×10
Beam to collimator 1	15.0	25.4
Collimator 2 slit[a]	NA	1.5×6.4
Beam to collimator 2	NA	12.7
Absorbing layers (μm)		
Be window	8	25.4
Au layer	0.02	0.02
Inactive Si layer	0.1	0.1
Mylar	100	NA

[a]The shorter dimension is parallel to the beam direction.

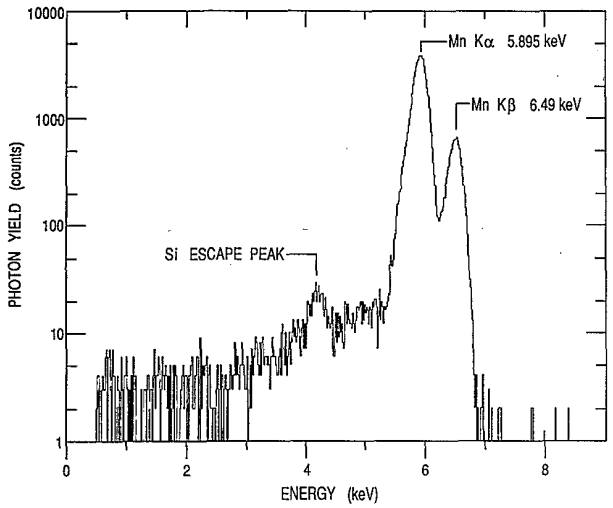

FIG. 3. An energy calibration spectrum from detector 3 for an ^{55}Fe radioactive source showing ^{54}Mn $K\alpha,K\beta$ lines [25,26]. The small peak on the low-energy tail of the Mn $K\alpha$ x-ray line arises from events in which the full x-ray energy is not deposited in the crystal because a Si K x ray ($K\alpha$, 1.74 keV; $K\beta$, 1.83 keV) escapes from the crystal.

The electronics for the experiment embodied energy measurement, pileup detection, coincidence detection, inhibit logic, and stepping motor control. It was also necessary to consider dead time carefully in the electronics and the computer data processing, and to provide normalization for the data at each foil position. Pileup events were handled by a combination of hardware and software. A multiple-hit TDC (time-to-digital converter) was used for this purpose. The TDC was gated for about 60 μs for each valid event to detect possible pileups that could modify an energy signal by more than 0.1%. Data from the TDC were recorded to tell whether or not a pileup was present and to measure the time difference between the two interfering signals. The time difference measurement enabled recovery of useful data when the data were replayed.

All fast timing signals except those going to the pileup detection electronics were gated by a single inhibit signal. When a valid event was established, further timing signals were inhibited until the computer finished processing the event. The inhibit logic was also used to gate out any undesired situations such as periods of lost beam or periods when the target foil was moving.

The charge collected in the beam dump was used to normalize the data. Digital pulses from an integrator of the Faraday cup current were counted and a preset number of pulses was required at each motor position. The output of the current integrator was also gated by the inhibit signal.

The computer set the foil position in a predefined sequence. In a typical run, data were taken for a collected charge of 3.8 nC for each of 18 foil positions. Each complete scan of the foil positions used in the experiment was made in approximately 20 minutes (about one minute per foil position). For the data reported here 37 scans of the decay curve were made, thus effectively averaging out any changes in the beam current or foil conditions. A precise linear position encoder measured the position of the target stage to an accuracy of 10 μm. The position measured by the encoder was digitized and recorded as part of the data stored for each event. The beam velocity was determined by measuring the time of flight over a 17-m-long path following the 3.4-mg/cm^2 stripper foil. The result was 7.368±0.007 cm/ns.

III. RESULTS

A. Coincidence data

The geometry for detectors 1 and 2 was chosen to optimize the detection of coincidence events from H-like two-photon decays. A lifetime measurement based on coincidence detection is desirable because a coincidence with the proper sum-energy provides a means for eliminating background and competition from He-like two-photon decays [10]. But the coincidence method requires high count rates in order to be successful. Unfortunately, very large pulses from neutrons or γ rays caused detectors 1 and 2 to malfunction if the beam current on target was raised above 100 pA (electrical). At this beam current, a total of 850 coincidences was detected for all motor positions combined. A sum-energy spectrum for these events is displayed in Fig. 4. It shows a clean peak structure at about 13.4 keV. These coincidences serve to identify two-photon emission, but the rate is too low to provide a precise lifetime measurement. If we had been able to use all the available beam we would have had over 50 000 coincidences in this time and this would have allowed a measurement to better than 1%. It is encouraging that at a beam current of 100 pA the rates in the detectors were low (100 Hz for detectors 1 and 2, and 10 Hz for detector 3), so that if the large saturation pulses (40 Hz for detectors 1 and 2, and 3 Hz for detector 3) could be eliminated or significantly reduced, the beam current could be raised by over an order of magnitude while still maintaining modest singles count rates in the individual detectors.

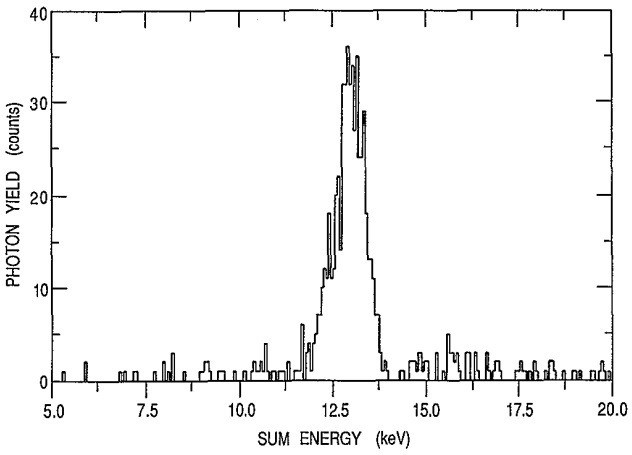

FIG. 4. A sum-energy spectrum from coincidences between detector 1 and detector 2. The peak energy is slightly lower than the $2\,^2S_{1/2}\rightarrow 1\,^2S_{1/2}$ transition energy of 13.43 keV because of the Doppler shift.

B. Decay rate measurement

Although the coincidence events were not usable for determining the lifetime, the singles spectra in detector 3 were clean and provided a good measurement of the $2\,^2S_{1/2}$ lifetime. The problems of background in the continuum and contributions from the two-photon decay of He-like Kr had to be handled carefully, and these limited the precision of the measurement. The spectra from detector 3 had relatively narrow lines, which allowed separation of the H-like and He-like single-photon lines. Also, the absolute efficiency of detector 3 had been measured, so the singles spectra from this detector provided an opportunity for making a direct determination of the branching ratio for the single-photon $M1$ decay of the one-electron $2\,^2S_{1/2}$ level.

Spectra from detector 3 are shown in Fig. 5 for three different foil positions. In Fig. 5(a) the peak near 13 keV is dominated by $M1$ photons from one-electron krypton. The two-photon decays ($2E1$) form a broad continuum with an energy span from 0 to 13.43 keV. These x rays are apparent in Fig. 5 (a) but are much reduced in Figs. 5(b) and 5(c) due to the fast $2\,^2S_{1/2}$ decay. Single-photon lines from transitions $nl' \rightarrow 2l$ in few-electron Kr ions contribute to the spectrum in the region from 2.5 to 4.5 keV. There is also a contribution to this region from fluorescence of molybdenum L x rays. As the foil is moved upbeam a line begins to be resolved on the low-energy side of the H-like $M1$ line, as shown in Fig. 5(b).

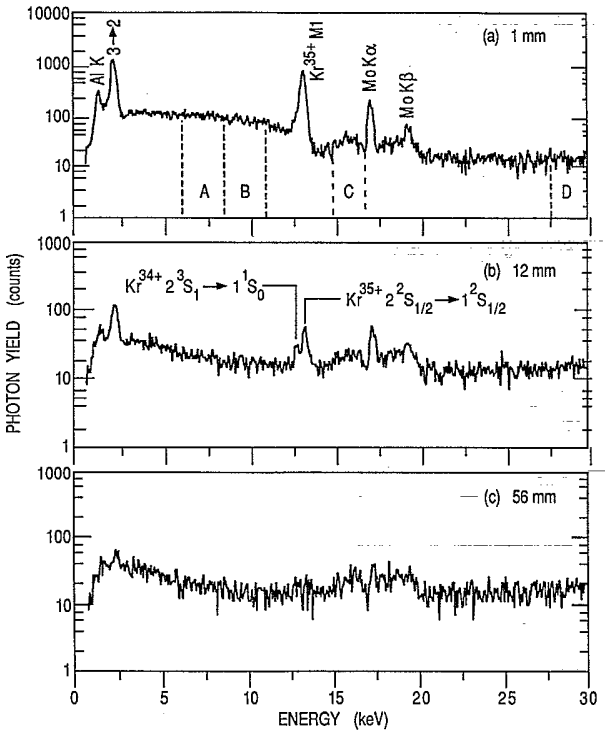

FIG. 5. Photon-energy spectra from detector 3 at different foil-detector distances as indicated in (a)–(c). The Mo $K\alpha,\beta$ and Al K x-ray peaks result from characteristic x rays from the shield, collimators, and target holder. The peak marked $3 \rightarrow 2$ is a combination of Mo L x rays and the $n=3 \rightarrow n=2$ transitions from one-, two-, and three-electron species.

This line comes from decays of the $n=2$ levels of He-like ions, which lie about 450 eV lower in energy. Figure 6 shows the lifetimes and energies of the low-lying He-like states. Both the $2\,^3S_1$ and the $2\,^3P_0$ levels are longer lived than the H-like $2\,^2S_{1/2}$ level. These lifetimes are 171 ps and 1.4 ns, respectively.

The lifetime of the $2\,^2S_{1/2}$ level was determined by analyzing the continuum region from 6.4 to 11.2 keV, which was divided into two regions (A and B). These were analyzed separately as a check for possible systematic errors. The lower boundary was chosen so as to be well separated from the $nl' \rightarrow 2l$ transitions and the high-energy boundary was chosen so as to avoid the He-like single-photon decays and the Si escape peak associated with the H-like $M1$ photons (see Fig. 3). At each motor position, the counts from these windows were corrected for pileup, cascades, and contributions from the two-photon decay of H-like ions. We also corrected the times determined from the foil position and beam velocity measurements for time dilation in order to obtain the decay time corresponding to each motor position.

Cascade repopulation of the $2\,^2S_{1/2}$ level can be reliably determined by noting that any cascade into $2\,^2S_{1/2}$ also has a branch to the $1\,^2S_{1/2}$ level with a known branching ratio [13] (see Fig. 7). Decays to the ground state from the np ($n>2$) levels contribute counts in the 15.9–17.9-keV region of the spectrum. We analyzed the more restricted region C of Fig. 5(a), which avoids the molybdenum line at 17.4 keV. Because of the lack of well-defined peaks, we consider the counts in region C after subtracting background (determined from region D) to be an upper limit to the ground-state cascades. From solutions to the rate equations governing cascade feeding [14] we determined corrections to be applied to the raw counts at each motor position. For example, this correction is about 0.6% at the first motor position. Since the correction amounts to an upper limit to the cascades, we increase the uncertainty in the result by the size of the correction and add an additional uncertainty to account for the neglect of the cascade counts in the region of the

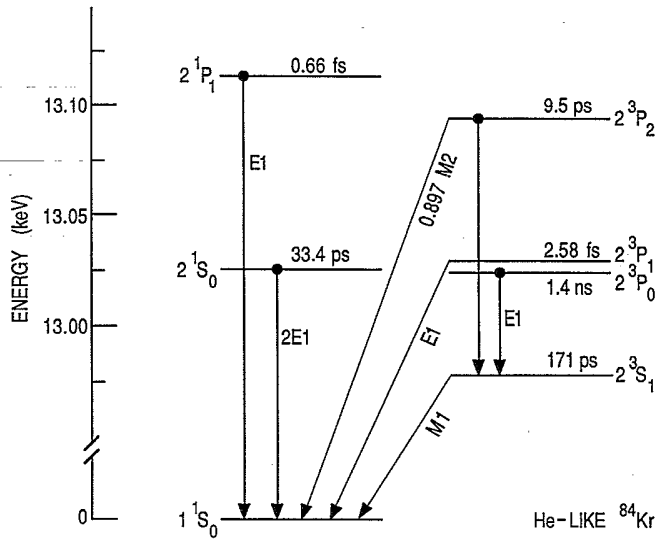

FIG. 6. Theoretical energy levels [27] and lifetimes [2,28] for low-lying levels of two-electron ^{84}K r^{34+}

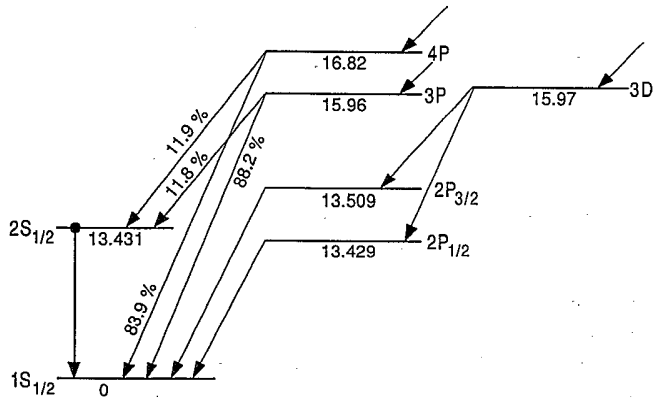

FIG. 7. Cascade scheme for one-electron $^{84}Kr^{35+}$ showing theoretical energies [29,30], and branching ratios [31].

molybdenum peak.

Capture of two electrons by the bare krypton ions in the target chamber can lead to the formation of He-like ions in the $2\,^1S_0$ state. Since this state also decays by two-photon emission with a similar lifetime (33.4 ps) and endpoint energy (13.03 keV), we cannot separate two-photon decays arising from the H-like and He-like decays. Our method for correcting for the He-like decay is to estimate the production rate of this state at the foil based on a measurement of the production rate of the He-like $2\,^3S_1$ level. We fit the region around the $M1$ peak with a linear background and two Gaussians of the same width separated by 450 eV. The He-like $M1$ counts determined from these fits at each motor position were then used to determine the rate of production of the $2\,^3S_1$ state at the foil. We assumed various values for the ratio of $2\,^1S_0$ production to $2\,^3S_1$ production at the foil and calculated a correction to the data assuming theoretical values for the lifetime and spectral distribution of the $2\,^1S_0$ state. If the ratio is taken to be $\frac{1}{3}$ corresponding to a statistical population of the levels, the correction is less than 0.7% at the first motor position and the fitted value of the $2\,^2S_{1/2}$ lifetime is changed by 0.2%. We do not have an independent determination of this ratio in our experiment, so we assume a statistical population and increase the uncertainty in the result by the size of this correction.

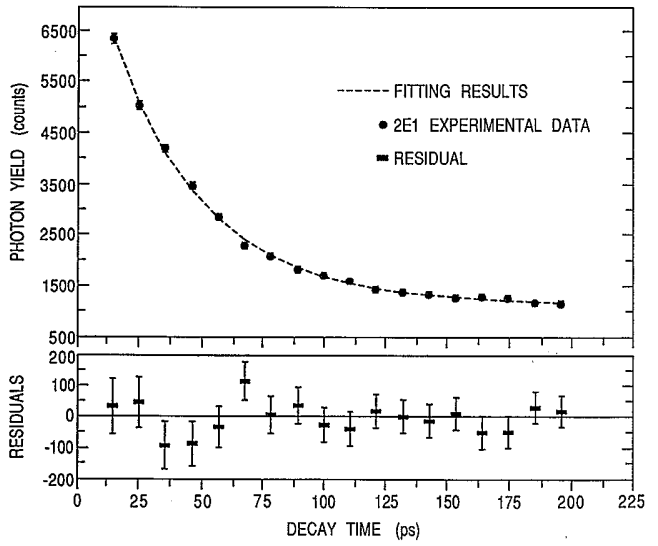

FIG. 8. Photon yield vs decay time for two-photon decays (regions A and B of Fig. 5). The residuals are the differences between experimental data and the fitted curve.

After all corrections were applied, the data were fitted to a single exponential plus a background. Several methods were employed to handle the background. One was to fit to an exponential plus a constant times the counts in region D of Fig. 5(a); another method was to fit an exponential plus a constant. These two methods each gave good fits to the data. A typical fit is shown in Fig. 8. The lifetimes extracted from the two methods agree to within the statistical uncertainty in the individual fits. The fits to regions A and B also agree to within the statistical uncertainty. The spread in these various fits results from our lack of knowledge of the true background and its dependence on foil-detector distance and photon energy. We take the lifetime to be the average over the results of these fits and increase our uncertainty to account for our lack of knowledge of the background. Other possible systematic effects including collisions with the background gas and continuum x rays arising from semi-Auger decays of Li-like ions were also considered. These processes were found to have a negligible effect on the measurement. Table II presents the results for the life-

TABLE II. Corrections and uncertainties

	Lifetime (ps)	Intensity (counts)[a]
	$2E1$ decay curve	
Fit result[b]	36.8 ± 0.75	7628±130
Cascades[c] to $2\,^2S_{1/2}$	±0.22	±46
He-like [c] $2\,^1S_0$	±0.26	±53
Background	±0.60	±61
Velocity and position	±0.07	
Totals[d]	36.8±1.4	7628±209
Corrected intensity[e]		9146±278
	$M1$ decay curve	
Fit result		4906±178
Cascades[c] to $2\,^2S_{1/2}$		±29
Fitting function		±74
Lifetime uncertainty		±98
Total[d]		4906±279
Corrected intensity[e]		5058±289

[a]Counts in detector 3 extrapolated to zero foil-detector separation. This corresponds to 142 nC (electrical) of beam at the Faraday cup.

[b]Fit to regions A and B of Fig. 5(a).

[c]Additional uncertainty (see text). Corrections were applied to the raw data before fitting.

[d]All uncertainties added in quadrature except for the background and fitting function uncertainties, which are added algebraically.

[e]Fitted intensities are divided by correction factors $f_{2E1}=0.834\pm0.011$ and $f_{M1}=0.970\pm0.006$. See Eqs. (5)–(8).

time of the $2\,^2S_{1/2}$ level and the intensity of the two-photon component.

C. Branching-ratio measurement

In order to determine the $M1$ branch of the $2\,^2S_{1/2}$ decay, the one-electron component of the 13.4-keV peak was found at each motor position by the two-Gaussian peak-fitting procedure. The resulting decay curve is dominated by the one-electron $M1$ decay, but there is also a longer-lived component due to cascades through the H-like $2p$ levels (see Fig. 7). After making a small correction for cascades into the $2\,^2S_{1/2}$ level we fitted the decay curve with various functions, including a single exponential plus a constant, and an exponential plus a power-law tail. The best results were obtained using a fit to two exponentials (see Fig. 9) with one lifetime fixed at the theoretical value for the $2\,^2S_{1/2}$ level. The lifetime of the second component was found to be about 140 ps. Although this fit does not determine the $2\,^2S_{1/2}$ state lifetime, it provides a reliable value for the intensity of the $M1$ component. We studied the dependence of the fit on the assumed value of the $2\,^2S_{1/2}$ state lifetime and increased our errors to correspond to the experimental uncertainty in this lifetime.

We correct the $M1$ intensity by dividing by the detector efficiency at 13.4 keV. Absolute efficiency calibration of Si(Li) x-ray detectors has been discussed by a number of authors [15–19]. For our detectors the silicon-sensitive depth is sufficient to completely absorb x rays in the energy region of interest (5–14 keV) and edge effects are minimized by collimation, so the efficiency is dominated by the absorption of x rays before reaching the active portion of the detector. Figure 10(b) is a plot of the calculated detection efficiency for x rays incident on detector 3, taking into account the various absorbing layers [20] listed in Table I. Additional absorption could be caused by the buildup of ice [17] on the cooled surface of the detector. Absolute efficiency calibration of detector 3 [21] shows agreement with the calculated efficiency and places an upper limit of 10 μm for an ice layer. Other processes that affect the detection efficiency include incomplete conversion of the x-ray energy and escape of silicon x rays. The probability for escape of a silicon K x ray increases with decreasing x-ray energy down to the silicon K edge. Cohen [16] found the ratio of the silicon escape peak to the photopeak increased from 0.14% at 8.6 keV to 0.8% at 3.7 keV. This is in rough agreement with the size of the escape peaks observable in our calibration spectra. Incomplete conversion leads to a low-energy tail extending to zero energy that reduces the full energy peak by about 2%.

We also correct the two-photon intensity by dividing by the factor

$$f_{2E1}(y_i,y_f,Z)=\frac{2\int_{y_i}^{y_f}\psi(y,Z)\epsilon(y)dy}{\int_0^1\psi(y,Z)dy}\ , \tag{5}$$

where

$$y=\frac{E}{E_0}\ , \tag{6}$$

E_0 is the end-point energy, and Z is the nuclear charge. The function $\psi(y,Z)$ is the spectral distribution defined

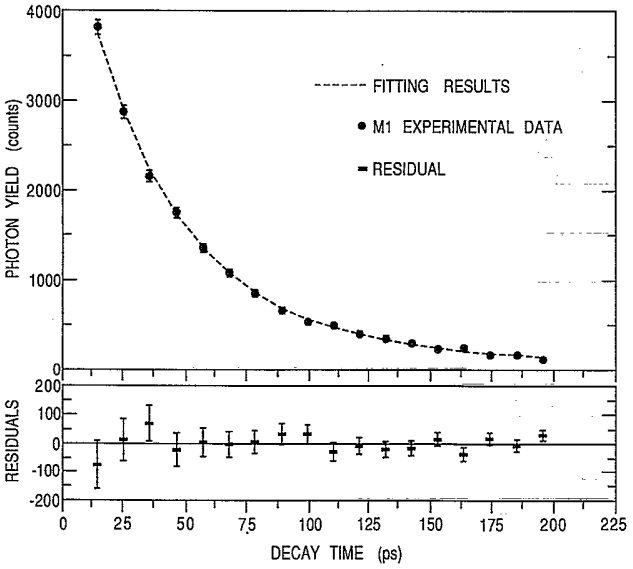

FIG. 9. Photon yields vs decay time for $M1$ peak in H-like krypton.

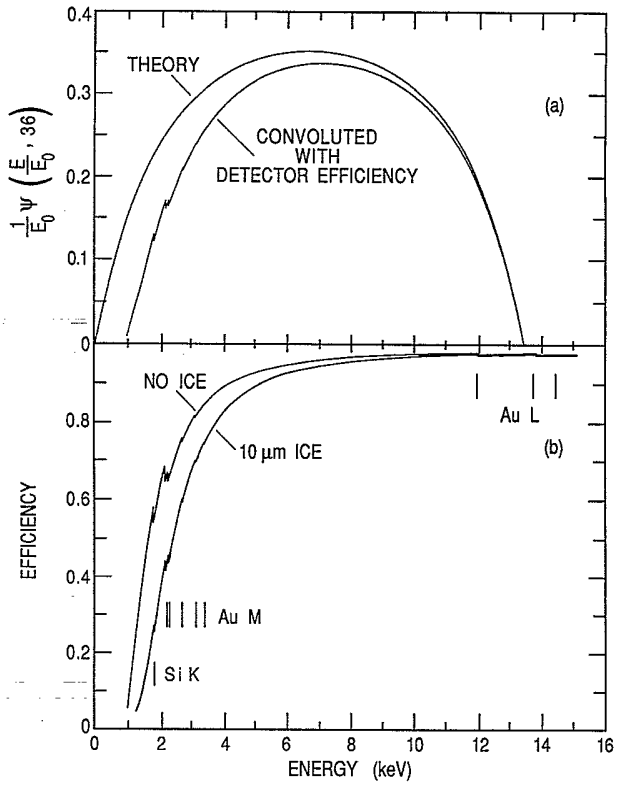

FIG. 10. (a) Theoretical two-photon spectral distribution for H-like $^{84}Kr^{35+}$ (see Ref. [3]). The parameter E_0 is the $2\,^2S_{1/2}\rightarrow 1\,^2S_{1/2}$ transition energy. The inner curve results from convolution with the detector efficiency. (b) A calculated detector efficiency for detector 3, assuming (i) no ice and (ii) 10-μm ice on the detector crystal surface.

by Johnson [3] and $\epsilon(y)$ is the detector efficiency as a function of energy, which is plotted in Fig. 10(b). We interpolated Johnson's results to obtain the spectral shape for the two-photon decays of H-like krypton. The result is plotted in Fig. 10(a).

Using the calculated detector efficiency, the two-photon correction factor found from Eq. (5) for regions A and B combined is

$$f_{2E1}=0.834\pm0.011\ , \tag{7}$$

and the detector efficiency for the $M1$ region is

$$f_{M1}=0.970\pm0.006\ . \tag{8}$$

In Table II we summarize the results and uncertainties for the lifetime and intensity measurements. The branching ratio b is calculated from the formula

$$b=\frac{\dfrac{I_{M1}}{f_{M1}}}{\dfrac{I_{M1}}{f_{M1}}+\dfrac{I_{2E1}}{f_{2E1}}}=0.356\pm0.015\ , \tag{9}$$

where I_{M1} and I_{2E1} are the uncorrected $M1$ and two-photon intensities. Combining this with our lifetime measurement, we find the corresponding magnetic-dipole decay rate $A_{M1}=9.68(55)\times10^9\ s^{-1}$ and the two-photon decay rate $A_{2E1}=1.750(78)\times10^{10}\ s^{-1}$.

IV. CONCLUSION

Parpia and Johnson [4] present fully relativistic calculations of both the two-photon and the $M1$ decay rates including finite-nuclear-size effects. Interpolating their results we obtain for krypton $A_{M1}=9.844\times10^9\ s^{-1}$ and $A_{2E1}=1.7184\times10^{10}\ s^{-1}$, where we have included a small correction for nuclear recoil [22,23]. The nuclear mass correction is negligible for krypton to the number of figures quoted. Goldman and Drake [5,6] have also calculated the relativistic corrections to the two-photon decay rate. Drake [2] fitted these results to an empirical formula good to within 0.005% up to $Z=92$, which includes finite-nuclear-mass and nuclear-recoil corrections. Using this formula for $Z=36$ gives $A_{2E1}=1.7181\times10^{10}\ s^{-1}$. The small difference between this result and that of Parpia and Johnson is less than the sensitivity of this experiment.

In Table III we summarize our experimental results and compare them with the theoretical values. There is good agreement between theory and experiment in all cases. In particular, our result for the $M1$ branching ratio agrees with the fully relativistic calculations but is about one standard deviation higher than the nonrelativistic result.

TABLE III. Experimental and theoretical results for the decay rate of the $2\,^2S_{1/2}$ level H-like $^{84}Kr^{35+}$.

	Experiment	Theory	NR theory[a]
Lifetime (ps)	36.8±1.4	37.008	36.982
$M1$ branching ratio	0.356±0.015	0.3643	0.3375
A_{M1} ($10^9\ s^{-1}$)	9.68±0.55	9.844[b]	9.126
A_{2E1} ($10^{10}\ s^{-1}$)	1.750±0.078	1.7184[b]	1.7914
		1.7181[c]	

[a]See Eqs. (1)–(3).
[b]Reference [4] with nuclear recoil correction Refs. [22,23].
[c]Reference [2].

It is clearly desirable to improve the precision of this measurement. The major problems to be overcome are (i) the background in the continuum region, (ii) contributions from He-like two-photon decays, and (iii) Yrast cascades through the $2p$ levels. The first two of these could be solved immediately by using the coincidence technique. The requirement of a coincidence with the proper sum-energy eliminates problems from background and He-like two-photon decays. This technique has produced 1% lifetime measurements of two-photon decays in H-like and He-like nickel [10,24] using lower-energy beams (11 MeV/amu) from Argonne's ATLAS accelerator. In order to get sufficient two-photon coincidence rates for a viable experiment, the background nuclear emissions encountered in this experiment must be reduced. This will require improvements to the shielding of the detectors and better beam collimation. Also, a study of the beam-energy dependence of both the background and the yield of $2s$ states may point to more optimum experimental conditions. The third problem, Yrast cascades which complicate interpretation of the $M1$ line, could be handled by adding a crystal spectrometer to the experimental setup that could separately resolve the lines from the $2\,^2P_{1/2}$, $2\,^2P_{3/2}$, and $2\,^2S_{1/2}$ levels. Such experimental improvements could produce a measurement of the $M1$ branching ratio at the 1% level, which would provide a definitive test of the relativistic corrections.

ACKNOWLEDGMENTS

We are indebted to the staff of NSCL for excellent technical assistance during this experiment. We particularly thank N. Anantaraman, D. Sanderson, R. Blue, R. Fox, J. Rugis, and R. Ronningen. This work was supported by the U. S. Department of Energy Office of Basic Energy Sciences under Contract Nos. W-31-109-ENG-38, DE-FG02-92ER14283 (University of Notre Dame), and DE-FG05-88ER13958 (University of Toledo). NSCL is supported by the National Science Foundation.

*Present address: Physics Division, Argonne National Laboratory, Argonne, IL 60439.

[1] S. Klarsfeld, Phys. Lett. **30A**, 382 (1969).
[2] G. W. F. Drake, Phys. Rev. A **34**, 2871 (1986).
[3] W. R. Johnson, Phys. Rev. Lett. **29**, 1123 (1972).
[4] F. A. Parpia and W. R. Johnson, Phys. Rev. A **26**, 1142 (1982).
[5] S. P. Goldman and G. W. F. Drake, Phys. Rev. A **24**, 183 (1981).
[6] S. P. Goldman, Phys. Rev. A **40**, 1185 (1989).

[7] E. A. Hinds, J. E. Clendenin, and R. Novick, Phys. Rev. A **17**, 670 (1978).
[8] M. H. Prior, Phys. Rev. Lett. **29**, 611 (1972).
[9] H. Gould and R. Marrus, Phys. Rev. A **28**, 2001 (1983).
[10] R. W. Dunford, M. Hass, E. Bakke, H. G. Berry, C. J. Liu, M. L. A. Raphaelian, and L. J. Curtis, Phys. Rev. Lett. **62**, 2809 (1989).
[11] C. L. Cocke, B. Curnutte, J. R. MacDonald, J. A. Bednar, and R. Marrus, Phys. Rev. A **9**, 2242 (1974).
[12] R. Marrus and R. W. Schmieder, Phys. Rev. A **5**, 1160 (1972).
[13] H. A. Bethe and E. E. Salpeter, *Quantum Mechanics of One- and Two-Electron Atoms* (Springer-Verlag, Berlin, 1957).
[14] L. J. Curtis, Am. J. Phys. **36**, 1123 (1968).
[15] J. S. Hansen, J. C. McGeorge, D. Nix, W. D. Schmidt-Ott, I. Unus, and R. W. Fink, Nucl. Instrum. Methods **106**, 365 (1973).
[16] D. D. Cohen, Nucl. Instrum. Methods **178**, 481 (1980).
[17] D. D. Cohen, Nucl. Instrum. Methods **193**, 15 (1982).
[18] D. D. Cohen, Nucl. Instrum. Methods **A267**, 492 (1988).
[19] Z. B. Alfassi and R. Nothman, Nucl. Instrum. Methods **143**, 57 (1977).
[20] E. Storm and H. I. Israel, Nucl Data Tables **A7**, 565 (1970).
[21] M. Paul, I. Ahmad, and W. Kutschera, Z. Phys. A **340**, 249 (1991).
[22] R. Bacher, Z. Phys. A **315**, 135 (1984).
[23] Z. Fried and A. D. Martin, Nuovo Cimento **29**, 574 (1963).
[24] R. W. Dunford, H. G. Berry, D. A. Church, T. P. Dinneen, M. Hass, C. J. Liu, N. Berrah-Mansour, R. C. Pardo, M. L. A. Raphaelian, L. Young, B. J. Zabransky, and L. J. Curtis, Z. Phys. D **21**, S13 (1991).
[25] J. A. Bearden, Rev. Mod. Phys. **39**, 78 (1967).
[26] J. A. Bearden and A. F. Burr, Rev. Mod. Phys. **39**, 125 (1967).
[27] G. W. F. Drake, Can. J. Phys. **66**, 586 (1988).
[28] C. D. Lin, W. R. Johnson, and A. Dalgarno, Phys. Rev. A **15**, 154 (1977).
[29] W. R. Johnson and G. Soff, At. Data Nucl. Data Tables **33**, 405 (1985).
[30] G. W. Erickson, J. Phys. Chem. Ref. Data **6**, 867 (1977).
[31] W. L. Wiese, M. W. Smith, and B. M. Glennon, *Atomic Transition Probabilities* (U.S. GPO Washington, DC, 1966).